Performance Modeling for the RAVEN Multi-Object Adaptive Optics Demonstrator

DAVID R. ANDERSEN,[1] KATE J. JACKSON,[2] CÉLIA BLAIN,[2] COLIN BRADLEY,[2] CARLOS CORREIA,[1] MEGURU ITO,[2] OLIVIER LARDIÈRE,[2] AND JEAN-PIERRE VÉRAN[1]

ABSTRACT. RAVEN will be a Multi-Object Adaptive Optics (MOAO) technology and science demonstrator on the Subaru telescope. The baseline design calls for three natural guide star (NGS) wavefront sensors (WFS) and two science pickoff arms that will patrol a ∼2′ diameter field of regard (FOR). Sky coverage is an important consideration, because RAVEN is both a technical and science demonstrator. Early-stage simulation of RAVEN's performance is critical in establishing that the key science requirement can be met. That is, 30% of the energy of an unresolved point-spread function (PSF) be ensquared within a 140 mas slit using existing WFS camera and deformable mirror (DM) technology. The system was simulated with two independent modeling tools, MAOS and OOMAO, which were in excellent agreement. It was established that RAVEN will be an order 10×10 adaptive optics (AO) system by examining the tradeoffs between performance, sky coverage, and WFS field of view. The 30% ensquared-energy (EE) requirement will be met with three NGSs and will exceed 40% if the Subaru Laser Guide Star (LGS) is used on-axis (assuming median image quality). This is also true for NGSs as faint as $m_R = 14.5$.

Online material: color figures

1. INTRODUCTION

The dawn of Extremely Large Telescopes (ELTs) is upon us. The Thirty Meter Telescope (TMT; Nelson 2008), the European-ELT (E-ELT; Kissler-Patig 2010), and the Giant Magellan Telescope (GMT; Shectman & Johns 2010) are all approaching their construction phase. Near-infrared spectrographs with 20 or more deployable integral field units over a 5 to 10′ FOR, assisted by MOAO, are highly desirable potential instruments on ELTs, because they can be used to address major areas in their top-level science cases. These MOAO integral field spectrographs (IFSs) are ideally suited for studying the evolution of galaxies from first light to the era of peak star formation. However, use of such an instrument will not be limited to extragalactic astronomers; any astronomer seeking multi-object spectroscopy that takes advantage of the "D^4" sensitivity gain provided by AO will consider a MOAO IFS to be a workhorse instrument. Infrared Multi-Object Spectrograph (IRMOS; Gavel et al. 2006; Andersen et al. 2006) and Extremely Large Telescope Adaptive Optics for Galaxy Evolution (EAGLE; Cuby et al. 2010) instrument are two examples of MOAO + IFS instrument concepts for, respectively, the TMT and the E-ELT.

To achieve correction over a large FOR, a MOAO system must overcome an effect known as "anisoplanatism." For a given telescope pointing, the light from a distant source is perturbed by the turbulence in a cylinder (with a diameter the size of the telescope primary mirror). Light from a nearby source will pass through an overlapping, but nonidentical, cylinder of turbulence on its way to the telescope. In a classical AO system, a single WFS will pick off light from a single, relatively bright, point source, and a DM will be commanded to take the appropriate shape to null-out the wavefront error induced by the turbulence along a single line of sight (within a single cylinder). The AO correction for a different source will not be as good, because it will be viewed through a slightly different cylinder of turbulence. Definitions vary slightly, but the isoplanatic angle, θ_0, can be thought of as the angular distance from the guide star at which the Strehl ratio drops significantly. The quantity $\theta_0 \propto \lambda^{6/5}$ and is typically 10″ in the H band (for a corrected field of view [FOV] of ∼20″).

There are two approaches for enlarging the isoplanatic angle. One approach is to place multiple DMs in series, each conjugate to a different atmospheric altitude. This multiconjugate AO (MCAO; Johnstron & Welsh 1991; Ragazzoni 1999; Flicker et al. 2000) approach can be used to enlarge the FOV to sizes of an arcminute or two, but the performance will ultimately still be limited by generalized anisoplanatism (Rigaut et al. 2000). The FOV can be further enlarged by adding even more DMs in series, to remove the turbulence generated at even more

---

[1] National Research Council, Herzberg Institute of Astrophysics, 5071 West Saanich Road, Victoria, BC V9E 2E7, Canada.

[2] Adaptive Optics Laboratory, Department of Mechanical Engineering, University of Victoria, Victoria, BC V8P 5C2; david.andersen@nrc-cnrc.gc.ca.

atmospheric heights, but the complexity of the MCAO system rises (and the throughput falls) with each additional DM relay.

MOAO is a parallel approach that promises to increase the field over which AO corrections can be applied to 5 or even 10′ (Hammer et al. 2002). MOAO systems use the fact that there are only a limited number of interesting targets in a given FOR, and astronomers will be happy if AO corrections are made only in those directions. If a sufficiently accurate measurement is made of the turbulent volume over a telescope, one can place a probe with an embedded DM anywhere in the FOR and make the optimal turbulence correction for that position. Making a measurement of the turbulent volume requires information from multiple WFSs locked on multiple guide stars that probe different lines of sight through the atmosphere. Once the information from these multiple WFSs is combined into a single tomographic model of the turbulence (Tokovinin et al. 2001), it is straightforward to imagine multiple science pickoffs in parallel, each incorporating its own DM, feeding multiple IFSs. Falcon for VLT was the first proposed MOAO IFS (Hammer et al. 2002; Puech et al. 2006), and it has served as a model for the more recent IRMOS and EAGLE studies for ELTs.

Many of the challenges involved in designing a MOAO system, such as the use of tomography (Ragazzoni et al. 1999; Costille et al. 2010; Ammons et al. 2010), microelectromechanical system (MEMS) mirrors (Morzinski et al 2010), and woofer-tweeter control (Jackson et al. 2010), have all been demonstrated to work in different laboratory settings and are included in advanced instrument concepts. Open-loop (OL) control is perhaps the greatest risk to MOAO, however, partly because it is the biggest unknown. In an AO system with OL control, the WFSs do not sense the correction applied by the DM. Instead, the WFSs sense the full turbulent phase of the atmosphere and the DMs are commanded to take the appropriate shape without benefit of any feedback. While OL control is not a new idea (Primmerman et al. [1991] used so-called go-to adaptive optics to make corrections and take science images immediately following pulses from a laser guide star with a low duty cycle), interest in implementing open-loop control on-sky has been reinvigorated in the past few years, as we shall see in the next section. After all, OL control introduces unique requirements on an AO system: the WFS needs to have a high dynamic range; effects of DM hysteresis and nonlinearity need to be mitigated; and, finally, alignment and calibration become more challenging.

1.1. MOAO Demonstrators

While the risks associated with MOAO IFSs have kept proposed VLT and ELT instruments on the drawing board, the scientific promise is so great that multiple on-sky demonstrators have been developed. The Visible Light Laser Guidestar Experiments (ViLLaGEs; Gavel et al. 2008; Ammons et al. 2008) is a MEMS DM-based AO testbed on the Nickel 1 m telescope at Lick Observatory. ViLLaGEs carried out on-axis experiments in both closed and open loop with NGSs and LGSs. It was the first on-sky experiment to successfully demonstrate open-loop control. ViLLaGEs is a test bed that is being employed to develop the Keck Next Generation Adaptive Optics (NGAO; Wizinowich et al. 2010; Ammons et al. 2010) instrument, which is a tomographic, high-order, open-loop AO system.

The Victoria Open Loop Testbed (VOLT; Andersen et al. 2009) was an experiment aimed at distilling the problems of open-loop control into a simple experiment. VOLT demonstrated open-loop control in the laboratory and on-sky at the Dominion Astrophysical Observatory 1.2 m telescope using a simple on-axis NGS system (Andersen et al. 2008). Both the VOLT and ViLLaGEs open-loop AO demonstrators performed below expectations at low temporal frequencies, which seems to indicate that small misalignments in open-loop AO systems may ultimately limit their performance. These experiences have led to a second generation of MOAO demonstrators that emphasize both calibration and alignment techniques.

CANARY is a MOAO demonstrator at the William Herschel Telescope (Vidal et al. 2010; Gendron et al. 2010; Morris et al. 2010) that is considered a pathfinder for EAGLE on the E-ELT. The goals of the CANARY project are to perform NGS-based (and, subsequently, LGS-based tomographic wavefront sensing), perform open-loop AO correction on-sky, and develop calibration and alignment techniques. This experiment saw first light in the fall of 2010 and achieved a MOAO Strehl ratio of 26% in the H band (Gendron et al. 2011). CANARY will ramp up to a full MOAO test bed with multiple LGSs by 2013. While the performance of CANARY at low temporal frequencies was improved, it still suffered in comparison with the performance in closed loop (E. Gendron 2011, private communication).

1.2. The RAVEN MOAO Demonstrator

RAVEN will be the first MOAO instrument on an 8 m class telescope feeding an AO-optimized science instrument, the Subaru Infrared Camera and Spectrograph (IRCS; Tokunaga et al. 1998).[3] RAVEN has many of the same technical aims as CANARY, but also has some significant differences. Figure 1 shows a functional block diagram for RAVEN.

RAVEN consists of nine main subsystems:

1. The deployable calibration unit (CU) is a telescope simulator and a turbulence generator. It contains an array of off-axis NGS sources and one on-axis LGS source. Light from the CU will feed the three OL WFSs, the LGS WFS, and two science arms. The three functions of the CU are to (1) help align other RAVEN subsystems, (2) calibrate the AO system (generate interaction matrices and measure field-dependent non–common-path aberrations), and (3) test the MOAO system by

---

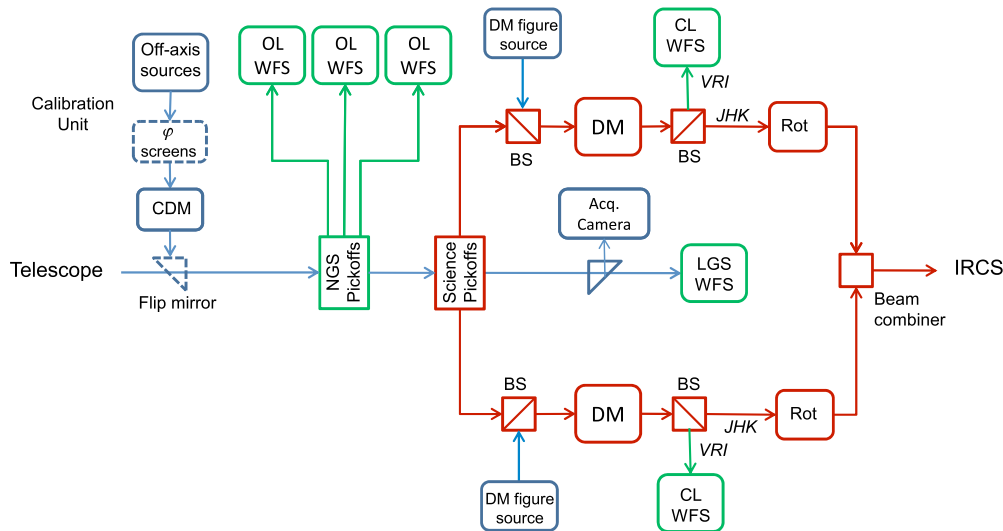[3] See http://www.naoj.org/Observing/Instruments/IRCS/.

FIG. 1.—Functional optical block diagram of RAVEN. Dashed blocks are deployable. RAVEN consists of nine main subsystems: the deployable calibration unit, the open-loop NGS WFSs, the science pickoffs, the science relays, the closed-loop NGS truth/figure WFSs, the beam combiner, the LGS WFS, and the acquisition camera. The real-time computer is not shown. See the electronic edition of the *PASP* for a color version of this figure.

including three phase screens (including a ground-conjugate DM inside the CU).

2. The three NGS OL WFSs are mounted on x–y translating stages to prevent the pupil from rotating on the WFS lenslet array with respect to the DMs.

3. RAVEN includes an on-axis LGS WFS, which will be fed by the Subaru sodium beacon in order to improve AO correction and/or the sky coverage (as discussed in § 3.5.2).

4. The science pickoff design consists of a mirror mounted on a r–θ arm, followed by a trombone mirror that keeps the path length constant.

5. The science relay for each arm contains a DM (which we expect to be a custom ALPAO DM with 11×11 actuators with a 25 mm aperture).

6. A figure source and closed-loop (CL) WFS share the science relay optical path and can be used to either (1) measure the shape of the DM using the figure source, (2) use the CL WFS as a truth WFS to help calibrate RAVEN or measure the MOAO performance, or (3) use the CL WFS as a classical AO system that uses the science target as the NGS.

7. After the science relay, light from both arms of the system is combined so that the common beam shares an identical exit pupil and provides two adjacent 4″ science fields to the single IRCS slit. The beam combiner also contains two K mirrors, which can rotate the images of the science targets so that extended objects can be properly aligned onto the slits.

8. An acquisition camera can be used to determine the telescope pointing and ensure that shadows of the probe arm fall over the NGSs and science targets.

9. Finally, pixels from the WFS detectors will be read by the RAVEN real-time computer (RTC) and transformed into a tomographic model of the atmosphere above the observatory. This tomographic model will be sampled in directions defined by the position of the science probes in the patrol field, and DM commands will be generated and applied.

The science gain achievable by RAVEN, in comparison with classical AO systems such as Subaru's AO188 (Minowa et al. 2010), will be modest, because RAVEN will only have two science channels. Nevertheless, the 8 m aperture of the Subaru telescope enables science that is not achievable on smaller telescopes, and RAVEN will be capable of delivering high ensquared energy into the IRCS slit. The combined technical and scientific aspects of MOAO that RAVEN will demonstrate are meant to excite the astronomical community and build support for future facility-class MOAO instruments with much larger multiplex advantages for either 8 m class telescopes or ELTs.

1.3. RAVEN Performance Modeling

MOAO has the potential to deliver near–diffraction-limited images to multiple small patches spread across a large FOR. One challenge of an MOAO system is that it is highly distributed. For RAVEN, light from three or four guide stars will be sensed by open-loop WFSs and a tomographic model of the atmosphere generated by the RTC. The RTC will then produce DM commands specific to the direction of the science pickoff arms. All of these actions are performed using OL control. Accurate knowledge of the science probe's placement in the focal plane and the relative alignment of the DM and WFS in the pupil plane is required.

2012 PASP, **124**:469–484

A broad swath of parameter space has been explored in order to determine if RAVEN can realistically meet the proposed performance requirements and deliver useful MOAO-corrected images to the Subaru IRCS spectrograph. As RAVEN was conceived to be a science-capable, NGS-only MOAO system, in addition to a technical demonstration, the AO architecture was designed such that it will deliver the desired performance when even faint guide stars are used. The addition of the single on-axis Subaru LGS to the NGS constellation improves performance and sky coverage, but does not eliminate the need for good performance with faint NGSs.

In this article, we assess the performance of the RAVEN MOAO system. In § 2, we describe MAOS (Multithreaded Adaptive Optics Simulator) and OOMAO (Object-Oriented MATLAB Adaptive Optics), the two simulation tools used in this study. In § 3, we describe the baseline system performance of RAVEN. This involves a description of the performance metrics, the derived atmospheric profiles, and the RAVEN ensquared-energy error budget. In § 4, we describe the trade studies that led us to our baseline design and describe RAVEN performance when used with different model atmospheres or at different zenith angles. Finally, we summarize our findings and present a road map of more detailed simulations that will be undertaken as we continue the development of RAVEN.

2. SIMULATION TOOLS

Our analysis was undertaken using two simulation platforms: MAOS and OOMAO.

2.1. MAOS

MAOS is a new C implementation of the tomographic AO simulator LAOS, which was written in MATLAB. This tool was created to efficiently run multithreaded simulations of large AO systems. MAOS is an ideal modeling tool for RAVEN, because it fully implements zonal tomography and can be configured for completely open-loop MOAO operations.[4]

The atmospheric turbulence in the model is composed of multiple phase screens that are located at different altitudes. These independent phase screens can either translate across the pupil, assuming a frozen flow for a given wind speed and direction, or MAOS can be run in a temporally uncorrelated mode in which each step of the simulation is temporally independent of the last (i.e., a simulated atmospheric phase is sensed by the WFSs and corrected by the DM in a single step). Running RAVEN simulations using this mode is advantageous, because the temporal errors are small (when run at a 500 Hz sampling frequency) compared with the tomographic errors, and the time-averaged PSF is more uniform. The resulting aberrations, due to

the simulated atmosphere, are sensed by multiple NGS (and LGS) Shack-Hartmann WFSs. MAOS can simulate the full physical optics WFS model that uses input pixel characteristics. Centroiding is accomplished using an optimal matched-filter (MF) estimation algorithm (Gilles & Ellerbroek 2006). The LGS WFS includes LGS elongation and cone effect. The tomographic wavefront reconstruction estimates the turbulence at several different heights from the open-loop gradients measured by the RAVEN WFSs, using a computationally efficient implementation of a minimum-variance reconstruction algorithm (Ellerbroek 2002). The reconstructed turbulent atmosphere is then projected, in MOAO mode, onto a DM corresponding to a given field direction. MAOS provides the user with numerous performance metrics, including rms wavefront error (both total and tip/tilt removed), Strehl ratio, and PSFs (defined at a given wavelength) for numerous field (DM) locations. Because MAOS is a highly optimized and proven tomographic Monte Carlo simulation platform, it was used for most simulations in this article.

2.2. OOMAO

The OOMAO modeling library is a set of MATLAB classes developed for the purpose of facilitating a clear and accessible end-to-end model of the RAVEN system. Objects from the different classes are assembled to perform numerical modeling of an AO system. OOMAO can be seen as an extension of the MATLAB language; overloaded MATLAB operators are used to propagate the wavefront through the system and to update the status of each object.[5]

Asterisms can be defined using the source class, with any number of guide stars in constellations specified by altitude-azimuth coordinates. The source class has a very important role in the OOMAO library, as it is the link between other classes. A source object carries a wavefront, both amplitude and phase, through the different objects representing the atmosphere, the telescope, the wavefront sensor, etc. Both NGS and LGS asterisms can be simulated. Currently all guide stars in the same asterism are defined with the same wavelength. Science source objects can be defined individually, assigned their own magnitude and wavelength, and placed at any point in the field of regard.

A modal tomography algorithm is implemented to reconstruct the phase, along with a thresholded center of gravity (CoG) to measure the spot positions on the WFSs. Using these methods, an end-to-end open-loop model of RAVEN has been developed with movable science objects in an adjustable asterism.

---

[4] MAOS is available from https://github.com/lianqiw/maos/. MAOS is written by Lianqi Wang and developed by Lianqi Wang, Luc Gilles, and Brent Ellerbroek of the TMT AO group.

[5] OOMAO is available from https://github.com/rconan/OOMAO. OOMAO was originally developed by Rodolphe Conan. Peter Hampton, Kate Jackson, and Olivier Lardière provided additional contributions.

Various classes have been modified to include functionalities that will facilitate the simulation of error sources such as misalignment. The DM class includes the ability to misalign the DM with respect to the optical path and other system components by specifying five parameters: horizontal and vertical displacements, rotation, tip, and tilt. Sensor noise has been included via the detector subclass. Parameters include readout gain, thermal dark signal, excess noise factor, charge capacity, and clock-induced charge, which allows for easy modeling of electron-multiplying CCDs (EMCCDs). The frame rate and exposure time are decoupled (i.e., the exposure time can be shorter than the time between frames). An aberration object uses Zernike modes to create a static or quasi-static aberration at a selected point in the optical path. This object can also be defined with a diameter that is much larger than that of the optical path so that larger optics with static aberration can be modeled easily. The `RotateDisplace` object shifts a specified image by a given number of pixels and then rotates by a given number of radians and is used within the aberration object to shift the large optical aberration across the smaller optical path. In this way, aberrations can be introduced at various points in the simulated optical path that are representative of potential errors in the real optical system. As shall be shown in the next section, OOMAO can reproduce the simulation results. This verification is important, as it builds confidence in the results from both simulation tools. It is especially important for us to trust the OOMAO simulations, because we intend to control real RAVEN hardware using OOMAO in the early stages of testing the instrument (before the RAVEN RTC is completed).

3. BASELINE SYSTEM PERFORMANCE OF RAVEN

As will be shown in the following sections, tomographic errors are the dominant factor limiting the performance of RAVEN. As a result, the performance will be highly dependent on the total amount of turbulence (and the distribution of turbulence as a function of altitude) and on the asterism of NGSs used to sense the turbulence. In this section, the metrics used to evaluate the performance are described, and the atmospheric profiles derived to use in simulation are outlined. The ensquared-energy budget of RAVEN and an estimate of the system's limiting magnitude are also presented.

3.1. Performance Metrics

RAVEN will feed the Subaru IRCS infrared imager and slit spectrograph. Since the majority of RAVEN science will be performed using the spectrograph, ensquared energy within the slit will be the most important performance metric. The IRCS echelle slit width is 140 mas wide, so ensquared energy (EE) within 140 mas at a wavelength of 1.65 μm (H band) was used as the primary performance metric. EE was evaluated primarily in the H band, because RAVEN will have a slightly higher thermal background in the K band relative to AO188, due to the

increase in the number of optical elements, and the performance in the H band will obviously be better than in the J band, due to the longer wavelength. The requirement for ensquared energy in the H band was set to 30% in order to match the requirement on ensquared energy from AO188.[6] By meeting this requirement, the multiplex advantage of RAVEN will be very nearly double that of AO188 (assuming that the science channel throughput of RAVEN continues to be greater than 40%).

Since 140 mas is significantly wider than the 42 mas diffraction-limited spot at 1.65 μm, RAVEN performance is most dependent on high spatial order wavefront errors (WFEs) and is relatively immune to modest errors at low spatial frequencies, including tip/tilt and focus. Therefore, another useful metric to evaluate in the simulations is the tip/tilt-removed WFE (other low-order aberrations, such as focus, could also be excluded, in principle). The Strehl ratio is also calculated (again measured at the H band), as is the total WFE, as these will be the quantities of interest when RAVEN is used with IRCS in imaging mode.

We have focused on setting the basic system parameters, such as system order, field of regard, and the limiting magnitude. To understand how performance varies with these and other parameters, we defined an asterism with three NGSs on a ring of 45″ radius and then evaluated the performance at multiple field points within that circle (in some simulations, a LGS WFS was included at the field center). The average performance is defined over points out to 30″ from the field center (excluding the field center when a LGS was used in the simulation).

3.2. Atmospheric Profiles

We derived atmospheric profiles for our RAVEN simulations by combining image-quality measurements from the Subaru Observatory and differential image motion monitor (DIMM) and multiaperture scintillation sensor (MASS) turbulence profiles measured by TMT at Mauna Kea. We used a realistic seven-layer profile generated from the TMT MASS/DIMM site survey MK 13N data (Els et al. 2009). To assemble representative profiles corresponding to the quartiles of this residual WFE, more than 10,000 individual MASS/DIMM profiles were sorted by uncorrectable residual WFEs (fitting-plus-lag error), and 10% of the profiles clustered around the quartiles were averaged (M. Schoeck 2011, private communication). While uncorrectable residual WFE is not equivalent to image quality (IQ), it is an acceptable surrogate. These three seven-layer turbulence profiles (starting 60 m above the MK 13N site), are given in Table 1.

We complemented these MASS/DIMM profile measurements with measures of Subaru IQ taken between 2000 and 2004 (Miyashita et al. 2004). Assuming an infinite outer scale,

---

[6] See the figures at http://www.naoj.org/Observing/Instruments/AO/performance.html.

TABLE 1
SUBARU ATMOSPHERIC PROFILES USED FOR RAVEN
PERFORMANCE MODELING

h (km)	J^2 25%	$\int C_n^2 dh$ 50%	(m$^{1/3}$) 75%
0	4.380×10^{-14}	9.419×10^{-14}	9.991×10^{-14}
0.06	7.345×10^{-14}	1.0318×10^{-13}	1.5225×10^{-13}
0.5	1.407×10^{-14}	3.190×10^{-14}	6.990×10^{-14}
1	4.882×10^{-15}	1.077×10^{-14}	2.919×10^{-14}
2	3.956×10^{-14}	1.233×10^{-14}	3.249×10^{-14}
4	1.744×10^{-14}	2.879×10^{-14}	4.212×10^{-14}
8	1.118×10^{-14}	2.264×10^{-14}	4.525×10^{-14}
16	2.612×10^{-14}	2.734×10^{-14}	3.538×10^{-14}
r_0 (500 nm)	19.4 cm	15.6 cm	12.1 cm
FWHM	0.53″	0.66″	0.85″

we determined the Fried parameter, r_0, for each quartile of IQ (Table 1).[7]

The image-quality–derived Fried parameter values are smaller than the TMT site-testing r_0 values derived from

$$r_0 = (16.7/\lambda^2 \cos^{-1}\gamma \sum_i J_i^2)^{-3/5}, \quad (1)$$

where $J_i^2 = \int C_n^2(h)dh$ over the ith layer, and γ is the zenith angle. We interpret these differences as being due to the local ground layer at the Subaru telescope, wind shake, and dome seeing. While not all of these PSF-broadening terms will necessarily follow a von Kármán spectrum, assuming that all the differences in r_0 are due to an additional ground-layer term that follows von Kármán is probably a conservative assumption. The first row, corresponding to 0 m, in Table 1 corresponds to this additional turbulence required to decrease the TMT site-testing–derived r_0 values to be in line with the Subaru image-quality measurements.[8]

This additional dome/ground seeing component in these profiles skews the fraction of the turbulence below 1 km to be greater than 60%. If the dome/ground seeing component is smaller and the free atmospheric turbulence is stronger (i.e., the isoplanatic angle is smaller), there will be a significant impact on RAVEN performance.

3.3. Simulated Performance

We simulated the performance of RAVEN using the median Subaru profile defined above. The three-NGS WFSs were on a 45″ radius ring and had 10 subapertures across the pupil. Section 4.3.1 shows the results of a system-order trade study that

---

[7] The true value of r_0 is probably overestimated by 10 to 20% by assuming an infinite outer scale (Martinez et al. 2010).

[8] In practice, the 0 and 60 m layers were combined into a single ground-layer profile in the simulations.

concludes that little improvement in performance can be gained for higher-order systems. A study of asterism diameter in § 4.1 also shows that there is limited improvement for guide star separations greater than 2′ diameter, as the footprints of the NGSs in the metapupils separate at relatively low altitudes, leaving much of the atmospheric turbulence unsensed and uncorrectable. The selected configuration parameters for the baseline design are given in Table 2.

Initial simulations of this baseline system show the best performance possible for RAVEN, since WFS noise and other implementation errors are not included (Fig. 2). The figure only shows the performance at points far from the NGSs. At the location of the NGSs, the WFE is ∼180 nm rms, which is consistent with the fitting error for a 11×11 order DM with a r_0 of 15.6 cm (145 nm). The fact that the wavefront error over most of the field is substantially higher than this (∼270 nm) suggests that the tomographic error is the dominant error source for RAVEN. It is due, in large part, to the incomplete overlap of the guide star footprints in the metapupils at higher altitudes, and this source of tomographic error will therefore decrease for larger-diameter telescopes (Tokovinin et al. 2001). Because the tomographic error was large, it was not essential to minimize the fitting error. Therefore, we adopted a relatively low order WFS (the 0.8 m d_0 value is quite large for most AO systems),

TABLE 2
RAVEN BASELINE CONFIGURATION PARAMETERS

| Parameters	Values
Telescope	
Diameter	8 m
Central obscuration	2 m
Atmosphere	
r_0 (500 nm)	15.6 cm
L_0	30 m
Zenith angle	0°
Profile	Subaru 50%
wind$_{GL}$	5.6 m s^{-1}
wind$_{top}$	19.1 m s^{-1} (at 8 km)
wind$_{dir}$	random
Sampling	1/64 m
Wavefront Sensor	
N_{NGS}	3
NGS radii	45″
Order	10×10
θ_{pix}	0.4″
N_{pix}	15
f_{sample}	500 Hz
λ_{WFS}	0.7 μm
DM	
Order	11×11
Stroke	Infinite
Influence functions	Bicubic spline
Evaluation	
N_{points}	49
λ_{evl}	1.65 μm
Sampling$_{PSF}$	$\lambda/4/D$
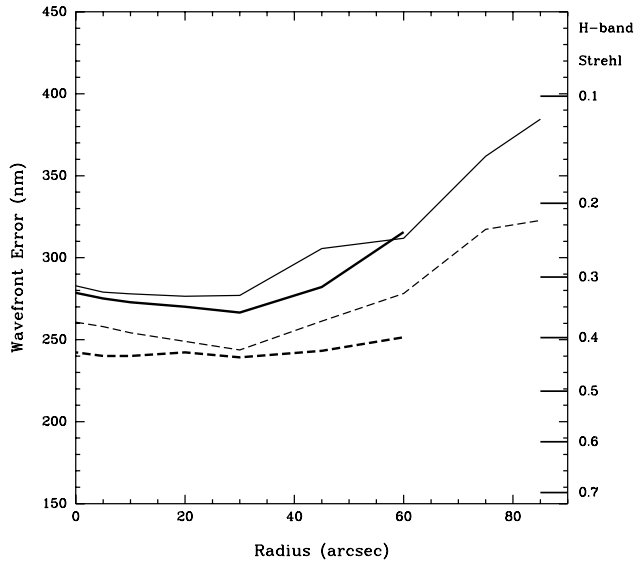
FIG. 2.—RAVEN performance for the baseline NGS-only configuration. Mean wavefront errors (all modes: *thin solid line*; tip/tilt removed: *thin dashed line*) vs. radius for field locations sampling half the focal plane for three NGSs on a 45″ radius ring. Mean fractional *H*-band EE (within 140 mas; *heavy dashed line*) and Strehl ratios (*heavy solid line*) measured from the PSFs are shown with the scale on the right (scaled to WFEs for comparison purposes by employing the Maréchal approximation, SR ≈ exp(−ω^2), where ω is the rms wavefront error in radians.) Only field locations not directly adjacent to the NGSs were considered.

which will allow us to maintain good corrections even when using a relatively faint NGS. This system should exceed the RAVEN 30% EE requirement by delivering ~40% EE within 140 mas, while delivering ~30% Strehl ratios over most positions in the field (in the absence of implementation errors discussed in § 3.4).

3.3.1. Comparison of MAOS and OOMAO Results

The predicted RAVEN performances from the MAOS and OOMAO simulations of the baseline system (Table 2) are in excellent agreement. Both simulation tools predicted a mean Strehl ratio of 30% for the points within 30″ of the field center. The two simulations also predicted an identical 43% ensquared energy in this area. Only the mean WFE differed slightly; MAOS predicted a slightly lower mean WFE of 290 nm, while OOMAO predicted 300 nm rms of WFE. The minimum WFE, reached at the NGS radius, is 220 nm rms. This is higher than the 180 nm rms best-case WFE obtained with MAOS. It is suspected that either the thresholded CoG used by OOMAO gives slightly poorer performance than the MF used in MAOS under these conditions, or the finite number of radial orders (8 in this case) used in the OOMAO tomographic reconstructor limits the simulated performance. Overall, however, the excellent agree-

ment between these two independent AO simulation tools provides us with confidence in our results and signals that both tools can be used interchangeably in our RAVEN simulations.

3.3.2. RAVEN Performance Gain from the Subaru LGS

RAVEN benefits greatly if it makes use of the Subaru LGS facility. The NGS WFSs can be moved farther out while still covering a majority of the metapupil at the top of the turbulent atmosphere (the NGS could be moved out onto a ~3′ diameter ring while maintaining some overlap with the LGS metapupil at 16 km). This will improve sky coverage, because the area over which NGS can be chosen while still meeting the RAVEN performance requirements will be substantially larger. Additionally, RAVEN can work with one LGS and just two NGSs (over a 2′ FOR). Again, this will markedly improve sky coverage if only two NGSs are required. The LGS is relatively bright; this can help compensate the AO performance of RAVEN when the other NGSs are faint, and superior performance can be achieved if three bright NGSs are found within a 2′ ring. Median WFE within a 2′ field will be ~230 nm (~190 nm of tip/tilt-removed wavefront error; Fig. 3). This corresponds to a large increase in ensquared energy (more than 50%) and Strehl ratio (greater than 50% up to 20″ from the LGS). These performance
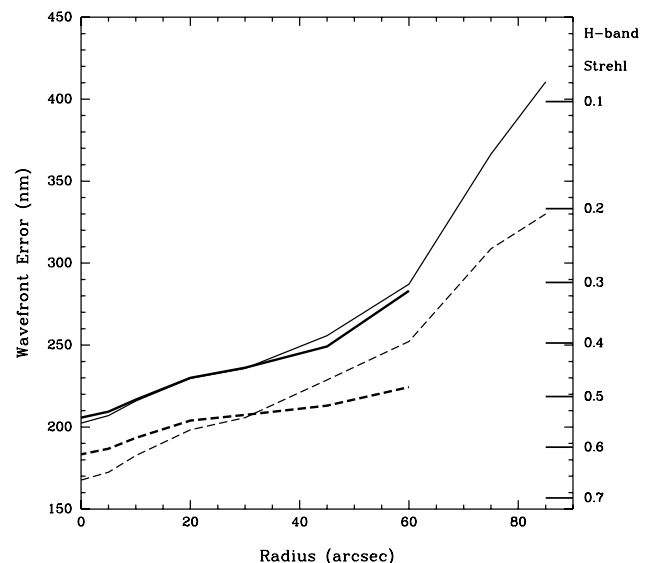

FIG. 3.—RAVEN performance for the baseline three NGSs plus on-axis LGS configuration. Mean wavefront errors (all modes: *thin solid line*; tip/tilt removed: *thin dashed line*) vs. radius for field points sampling half the focal plane for three NGSs on a 45″ radius ring and an on-axis LGS. Mean fractional *H*-band ensquared energy (within 140 mas; *heavy dashed line*) and Strehl ratios (*heavy solid line*) measured from the PSFs are shown with the scale on the right (scaled to the WFEs by the Maréchal approximation). Only field locations not directly adjacent to the NGSs were considered.
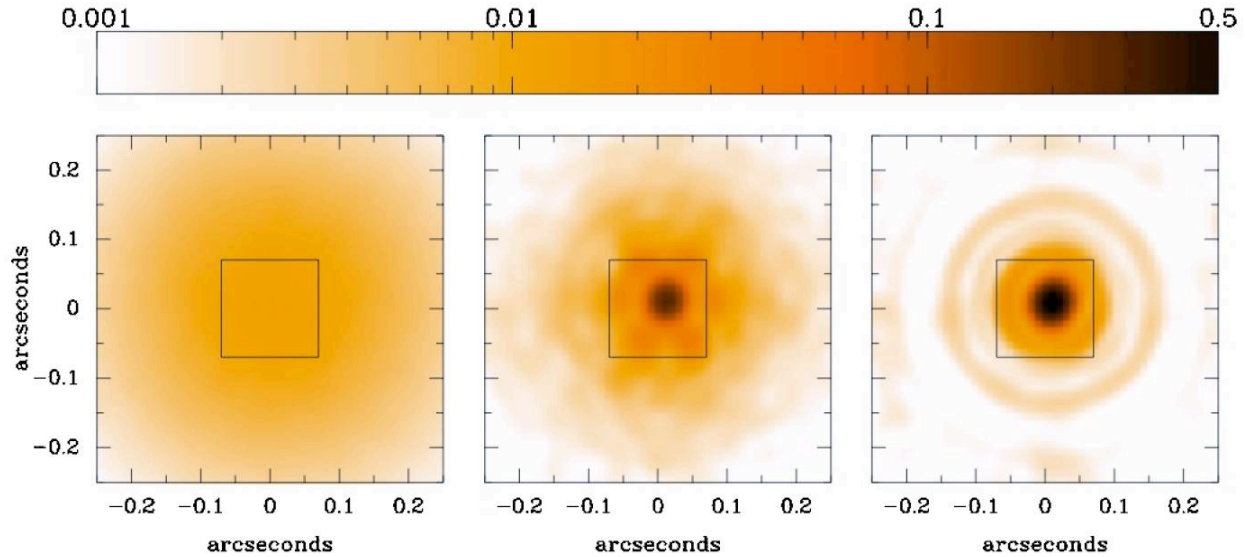
Fig. 4.—Simulated *H*-band PSFs in open-loop (*left*), RAVEN with three NGSs evaluated at the field center (*middle*), RAVEN with three NGSs and the LGS evaluated at the field center (LGS location; *right*). The box shows the 140 mas box in which ensquared energy is measured corresponding to the IRCS slit width; the simulated EEs are 10% with no AO, 40% with three NGSs, and 60% at the location of the LGS. All PSFs use the same stretch, with the scale corresponding to the peak flux of the perfect diffraction-limited PSF. See the electronic edition of the *PASP* for a color version of this figure.

predictions do not include the unmodelable implementation errors discussed in § 3.4.

A comparison of the open-loop (no AO correction) PSFs and the RAVEN-corrected PSFs (with and without the central LGS) is shown in Figure 4.

3.4. Error Budget

While the most important figure of merit for RAVEN is EE within a 140 mas slit, it is difficult to disentangle how potential sources of WFEs affect this metric. To give a sense of RAVEN performance, a WFE budget has been built in that it is easier for the expected contribution of different errors to be added together in quadrature. The high-order WFEs are of primary concern, because low-order errors (e.g., tip, tilt, and focus errors) will broaden the core of the PSF and not lead to significant losses in EE within a 140 mas box. The RAVEN WFE budget is listed in Table 3. The terms that are included in the simulations are described below, and then some additional implementation errors are listed; these include errors derived from laboratory tests of an ALPAO DM that is similar to the RAVEN science DMs.

Tomographic Error.—The dominant error term for RAVEN operating with just three NGSs will be the tomographic error. The median tomographic tip/tilt-removed WFE averaged over field points out to 40″ (not considering the center of the FOR when the LGS is considered) is 175 nm for RAVEN using just three NGSs on a 45″ radius ring and just 105 nm if the Subaru LGS is positioned at the center of the field. A certain fraction of this WFE is of relatively low order and will not substantially decrease the ensquared energy.

DM Fitting Error.—The 11×11 RAVEN DM cannot be used to fit high-order modes and will therefore contribute a fitting-error term, equal to roughly

TABLE 3
RAVEN TIP/TILT-REMOVED WAVEFRONT ERROR BUDGET

Term	Three NGSs	+LGS
Simulated WFE Terms (nm rms)		
Tip/tilt-removed tomography	175	105
DM fitting	155	145
WFS aliasing	103	112
WFS sampling	72	62
WFS noise ($m = 12$; $F_s = 500$ Hz)	54	83
WFS noise ($m = 14$; $F_s = 180$ Hz)	95	96
Simulated total ($m = 12$; $F_s = 500$ Hz)	271	236
Simulated total ($m = 14$; $F_s = 180$ Hz)	280	241
Simulated Ensquared Energy in 140 mas Slit		
Simulated EE ($m = 12$)	0.42	0.47
Simulated EE ($m = 14$)	0.40	0.46
Implementation WFE Terms (nm rms)		
Calibration +lag (-15 dB saturation; see text)	88	88
DM flattening	7	7
DM stability	27	27
DM repeatability	22	22
High-order optical errors	50	50
Implementation total WFE	107	107
Total WFE (nm rms)		
Total WFE ($m = 12$)	291	259
Total WFE ($m = 14$)	300	264
Total Ensquared Energy in 140 mas Slit		
Total EE ($m = 12$)	0.35	0.39
Total EE ($m = 14$)	0.33	0.38

$$\sigma_{\text{fit}}^2 \approx 0.25(d_0/r_0)^{5/3}, \qquad (2)$$

where d_0 is the interactuator spacing projected onto the primary mirror (0.8 m for the baseline system) and yields ~150 nm of WFE. This makes fitting error the next greatest contribution to the high-order WFE budget.

WFS Aliasing Error.—The large size of the subapertures on the WFS will also contribute an aliasing error that arises from high spatial frequency disturbances that affect the WFS signal. From simulations, we find that this error can be characterized by $\sigma_{\text{alias}}^2 \approx 0.1(d_0/r_0)^{5/3}$, or ~100 nm rms WFE, due to aliasing in the baseline system. This aliasing term will contribute to the scattering of light out of the PSF core and into the halo (and outside of the slit).

Taken together with the DM fitting error, the total generalized fitting error for RAVEN is large: approximately 180 nm rms. This is consistent with a generalized fitting error of roughly $\sigma^2 = 0.35(d_0/r_0)^{5/3}$ and is the same as for classical AO systems. While the generalized fitting error is equal to the tomographic term for the NGS-only case, the generalized fitting error dominates the high-order error budget when the LGS in included as well. We maintain the large subapertures and relatively low order of the RAVEN MOAO system in order to achieve a higher sky coverage and WFS dynamic range, as discussed in §§ 3.5 and 4.3, respectively.

WFS Sampling Error.—This term refers to the WFE that arises from the undersampling of the WFS spots by the RAVEN WFSs. The WFSs need to be undersampled, due to the limited number of pixels available to cover an order 10×10 system with a relatively large FOV. This term is dependent on the centroiding algorithm. We used the MF to determine this error. Other centroiding algorithms would have different WFS sampling and noise errors; we will choose a centroiding algorithm for RAVEN to minimize this error source.

WFS Noise Error.—The WFS noise was calculated from simulations with and without detector noise, photon noise, and sky background. This term obviously depends on guide star magnitude and the sampling rate. The noise errors quoted in Table 3 assume a 500 Hz sampling frequency for bright stars and a 180 Hz sampling frequency for fainter stars. This term can be reduced further if a slower sampling frequency is used at the expense of a larger lag error (which we include in the calibration-plus-lag error term of Table 3).

Implementation Errors.—There are a number of error sources that arise from sources that are not (yet) all simulated. These include the calibration-plus-lag error for an OL system; the DM flattening and go-to errors, as measured from the ALPAO DM 97 using a Zygo interferometer in the University of Victoria AO laboratory; and the high spatial frequency, uncorrectable errors on RAVEN optics. We made an educated guess that this last term will not exceed 50 nm rms WFE.

The top section of Table 3 contains the simulated error terms described above. The total errors for two different guide star brightnesses (with and without the addition of a fourth, constant-brightness, LGS) are derived by adding the individual terms together in quadrature. The ensquared energies measured from the simulated PSFs are also tabulated. The bottom section of the table includes implementation errors not included in the end-to-end simulations. The total WFE is a quadrature sum of the simulated and implementation errors. It should be noted that the error terms and their values are consistent with those reported by the CANARY team (Gendron et al. 2010). The ensquared energy, accounting for implementation errors, is calculated by assuming that the loss of Strehl ratio due to the high-order implementation errors will remove the same amount of light from the 140 mas box.

In this RAVEN performance budget, it was found that the implementation errors will further reduce the ensquared energy by ~15%. Most of this is due to the open-loop calibration and lag errors. We bundle these errors together by modeling the consequences of an open-loop rejection transfer function (RTF; the amount of turbulence that can be sensed and rejected as a function of frequency), which includes a constant wavefront error from misalignment or miscalibration. This constant error is manifested in the RTF as a plateau at low temporal frequencies; the amount of rejection over long timescales saturates. All open-loop AO systems to date have shown a RTF that saturates at low temporal frequencies. VOLT's RTF saturated at −15 dB, while other systems performed somewhat better (see § 4.6 for more details). In Table 3, a conservative estimate of 88 nm rms was made by assuming that the RTF of RAVEN will saturate at −15 dB. (This error only includes Zernike modes between 7 and 45. Errors on low-order Zernike modes will not substantially decrease the EE in 140 mas, and higher-order Zernike modes will not be fully corrected by RAVEN.) If a better calibration can be achieved, this saturation threshold may be reduced, perhaps to −25 dB, and the corresponding WFE would drop from 88 nm to ~40 nm. In this case, the implementation error would reduce the ensquared energy by just 10%. As long as no substantial implementation error remains unaccounted, the performance requirement of delivering 30% EE to the 140 mas spaxel will be met at zenith under median conditions. If the temporal error can be reduced through good calibration techniques, 40% EE can be achieved when using the Subaru LGS.

3.5. Limiting Magnitude of Asterism Guide Stars

The baseline RAVEN OL WFS detector is the EMCCD camera. These devices have the ability to operate with very high gain and low read noise. In this mode, the read noise can be made almost arbitrarily small; however, the background source plus background photon noise is effectively doubled. The signal-to-noise ratio (S/N) can be written as follows:

$$\text{S/N} = S_0/\sqrt{(2(S_D + (S_0 + B)) + (N_a/G)^2)}, \qquad (3)$$

where S_0 is the source counts (all measured in electrons); B is the background; S_D is effectively the dark current; N_a/G is effectively the read noise divided by the gain, and this ratio is chosen to be 0.1; and the S_D for the Andor cameras is actually a combination of two effects: the thermal dark signal,

$$D_t = 3.3 \times 10^6 t^2 e^{-9080/T}, \tag{4}$$

which can effectively be ignored for short exposure times when the cameras are cooled.

3.5.1. NGS-only Case

Using the noise characteristics of this EMCCD device, simulations were run using the baseline configuration. First, simulations of RAVEN using only NGSs were performed. Each simulation evaluated the performance of RAVEN as we varied the NGS magnitudes (Table 4). The performance started to degrade significantly by $m_R = 14.5$, but almost all of that performance could be regained if RAVEN were run slower, at 180 Hz. The servo-lag error did not start impacting the simulated WFEs, but it was decided to require that the open loop run at a rate of at least 180 Hz (for these simulations), because MAOS does not account for an OL RTF that plateaus at low temporal frequencies (§ 4.6). If RAVEN can be run at 180 Hz without loss in performance, the limiting magnitude becomes 1 mag fainter. Figure 5 shows the simulated PSFs for faint-magnitude NGSs in comparison with a bright star. The bright core is still evident for the $m_R = 14.5$ NGS asterism running at a sampling frequency of 180 Hz.

3.5.2. NGS with On-Axis LGS

RAVEN system performance improves in several ways with the addition of a central LGS. In addition to decreasing the tomographic error with the addition of another WFS (§ 3.3.2), RAVEN can use an asterism of three sources, including the LGS and just two NGSs. This will greatly enhance the sky coverage of RAVEN, as the NGS WFS probes can be moved 105″ away from the field center. Finally, the LGS can be used with three faint NGSs and still maintain significant EE. If it is assumed that the LGS is a $m_R = 11$ beacon (Y. Hayano 2011, private communication), and the three NGSs are $m_R = 15$, then RAVEN can still deliver an average EE > 40% (before losses due to implementation errors) over a 1′ diameter field (Fig. 6).

Sky coverage for RAVEN will be low, but the addition of the LGS to the NGS asterism will significantly improve the fraction of the sky that can be observed. As an example, consider a point with Galactic coordinates $(b, l) = (30, 0)$. Using the Besançon model of the Galaxy (Robin et al. 2003),[9] one finds that there are 750 stars per square degree with $R < 14.5$ (1040 stars per

---

[9] We generated synthetic catalogs of stars using http://model.obs-besancon.fr/.

TABLE 4
MEAN H-BAND PERFORMANCE OVER CENTRAL 30″ RADIUS AS FUNCTION OF NGS MAGNITUDE FOR NGS-ONLY CASE

m_R	$f_s = 500$ Hz		$f_s = 180$ Hz	
	EE$_{140}$	Strehl	EE$_{140}$	Strehl
Bright	0.43	0.30	…	…
10	0.43	0.30	…	…
12	0.42	0.27	…	…
14	0.36	0.17	…	…
14.5	0.33	0.12	0.40	0.18
15	0.29	0.08	0.37	0.14
15.5	…	…	0.34	0.11

square degree with $R < 15$). The probability that there are three stars with $R < 14.5$ in a 2′ diameter FOR is just 3%. This does not even account for asterisms that are unsuitable; in some cases, the science targets will not be inscribed within the potential NGS asterism, and therefore the tomographic error will be too great. If one just requires two NGSs with $R < 15$ within a 90″ diameter, with the third guide star provided by the LGS, the sky coverage increases to 10%. These asterisms are also more likely to be acceptable, as the observer will have greater flexibility in choosing the field orientation (and hence the on-sky coordinates of the LGS). If one can accept three NGSs with $R < 15$ within a 3′ diameter to be used in addition to the LGS, the potential sky coverage jumps to 34%. Again, a fraction of these potential asterisms may ultimately prove unacceptable for the given science targets, but at this Galactic latitude, the sky coverage will likely be 10 times higher with the LGS than without.

4. EXPLORING SIMULATION PARAMETER SPACE

We first focused on identifying and studying the major AO components: the WFSs and the DMs. Having established the basic AO architecture, the number of variables we explored was increased, and we included a closer examination of the possible consequences of open-loop temporal errors and different input model atmospheres.

4.1. Field of Regard with Respect to Asterism Geometry

Because RAVEN uses three NGS pickoffs that will patrol a FOR up to 3.5′ in diameter, we simulated RAVEN performance using three NGSs on rings of different diameters. As expected, a reduction in the diameter of the asterism leads to improved performance in the area inscribed within the asterism, with a rapid falloff in performance outside. This is due to an increased overlap of the NGS metapupils at higher altitudes, which leads to a better tomographic estimate of the turbulence above the telescope. Because of the great flexibility of the RAVEN NGS pickoffs, the possible asterism geometries are practically limitless. These simple simulations show, however, that once the guide
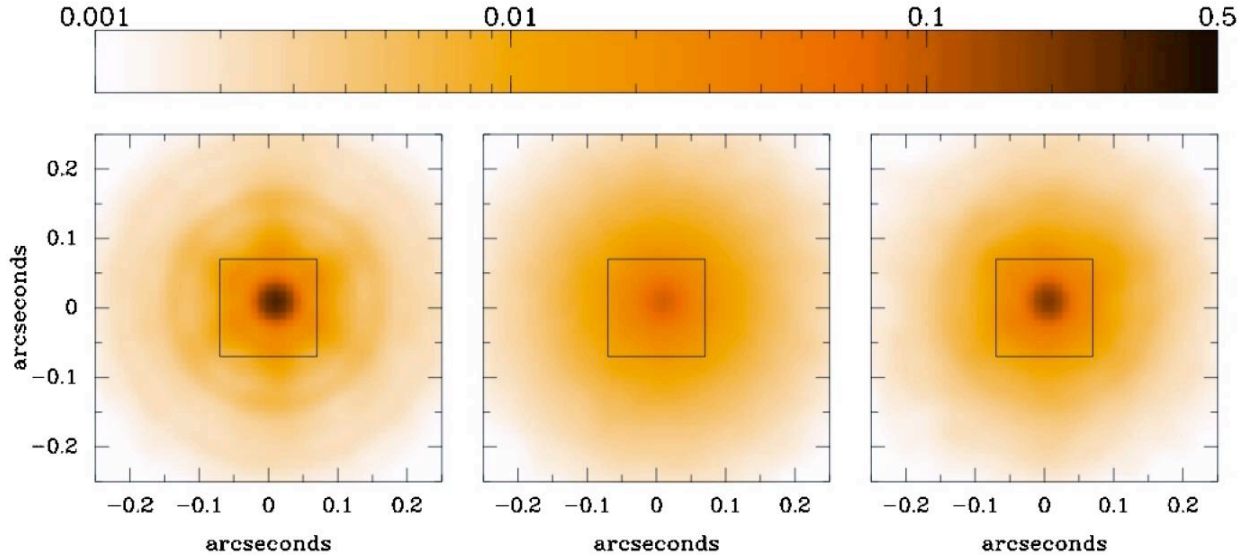
FIG. 5.—Comparison of field center PSFs for the three baseline NGS-only RAVEN simulations using guide stars with various magnitudes and sampling frequencies. *Left*: $m_R = 10$ and $f = 500$ Hz. *Middle*: $m_R = 14.5$ and $f = 500$ Hz. *Right*: $m_R = 14.5$ and $f = 180$ Hz. In the last of these cases, the core of the PSF is still present and a large fraction of the PSF energy remains within 140 mas (*boxed area*). See the electronic edition of the *PASP* for a color version of this figure.
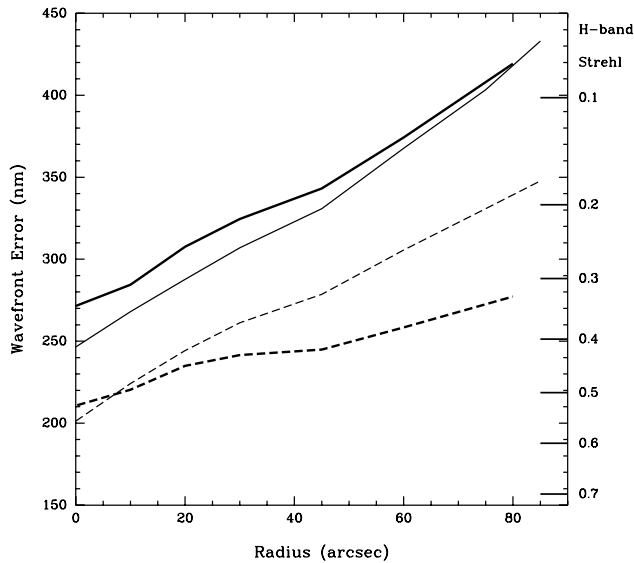

FIG. 6.—RAVEN performance for the three NGSs plus central LGS configuration when all three NGSs are faint ($m_R = 15$) and the sampling frequency is reduced to 180 Hz. Wavefront errors (all modes: *thin solid line*; tip/tilt removed: *thin dashed line*) vs. radius for evaluation points covering half the FOR for three NGSs on a 45″ radius ring. Mean fractional ensquared energy (within 140 mas; *thick dashed line*) and Strehl ratios (*thick solid line*) measured from the PSFs are shown with the scale on the right (scaled to the WFEs by the Maréchal approximation). Only field locations not directly adjacent to the NGSs were considered. The performance requirements of RAVEN should be met even when $m_R = 15$ guide stars are used with the LGS.

stars are separated by 2′, the performance becomes very uniform within that diameter (Table 5).

4.2. Enhanced Reconstruction and Control in Open Loop

RAVEN's performance and sky coverage could be improved by enhanced reconstruction and control techniques. Furthermore, it is believed that these methods will be critical to the success of future MOAO instruments on ELTs. Therefore, we advocate the use of RAVEN as a demonstrator in two areas of foremost importance for tomographic AO in general and MOAO in particular:

1. Operation in open loop makes it straightforward to use minimum pupil-integrated residual phase reconstructors (no temporal dynamics involved) in which the von Kármán spectrum is used as a priori knowledge for the volumetric estimation.

TABLE 5
MEAN H-BAND PERFORMANCE OVER CENTRAL 15″ RADIUS
AS FUNCTION OF ASTERISM DIAMETER

Asterism diameter (arcsec)	Strehl ratio	Ensquared energy	WFE (nm)
30	0.41	0.47	256
45	0.41	0.46	256
60	0.39	0.46	260
90	0.30	0.43	302
120	0.27	0.42	311

In closed loop, however, to make use of this information, a technique called pseudo–open-loop control has been proposed, consisting of converting the closed-loop measurements back to open-loop by adding in the DM contribution (Gilles & Ellerbroek 2008). Clearly, this is now avoided. It thus makes RAVEN a perfect candidate to demonstrate the algorithms developed for closed-loop AO in a much more favorable terrain. Testing and use of high-performance iterative phase reconstructors as the conjugate gradient and block Gauss-Seidel have been pursued. We are currently assessing the optimal number of iterations and the real-time requirements for their implementation. Iterative algorithms embody an alternative to current vector-matrix-multiply reconstructors that use the generalized inverse of the interaction matrix between measurements and voltages. In addition, since no explicit inverse matrix is computed, iterative methods are more suitable to on-the-fly updates from telemetry and calibration data sets. Testing and implementation will have a great impact in establishing real-time performance metrics and suitability for facility-size MOAO systems and in anchoring simulations to a real-world demonstrator as a precursor of AO for ELTs.

2. The OL control of the DMs also calls for novel temporal filtering approaches. Section 3.4 shows that the DM stability and repeatability (go-to error) is suitable for OL control, but this can be further enhanced by improving the model of the DM deformation (Guzmán et al. 2008). The application of minimum-variance techniques makes perfect applicative sense, and much insight has already been gained in using these techniques in standard closed-loop AO. They can potentially further reduce the servo-lag errors by embedding a full description of the delays (integer or fractional multiple of the sensing frame rate), the WFS and DM temporal dynamics, and the spatiotemporal properties of the disturbances (atmospheric phase, windshake, vibrations, and non–common-path aberrations).

The RAVEN team is currently tackling these issues, in the prospect of enhancing overall performance to increase sky coverage for full exploitation of RAVEN's capabilities.

4.3. WFS Simulations

The Andor iXon X3 860 camera, which uses a 128×128 pixel EMCCD, was selected as the WFS detector for the following reasons: this camera has low read noise, can be read out at rates up to 500 frames per second, and is an affordable choice for a MOAO demonstrator. The drawback of the camera is the number of pixels. OL WFSs need a high dynamic range. Choices had to be made regarding the order of the AO system, the WFS FOV, and the pixel scale, and their impacts on performance and sky coverage had to be understood.

4.3.1. System Order

A critical system design parameter is the order of the MOAO system (i.e., the number of subapertures across the WFS and

number of actuators across the diameter of the DM). Three major factors were important:

1. A commitment to producing an instrument that will deliver science data from IRCS to astronomers has been made, so sky coverage is a driving concern. Larger subapertures will allow the WFSs to work with fainter stars (as shown in § 3.5).

2. The system should not be limited in performance by fitting error if it can be avoided.

3. A tertiary concern is that if the number of subapertures were large, the number of pixels per subaperture will be limited.

A number of simulations were performed that evaluated the performance with different numbers of subapertures. The simulations were performed for the case of the NGS + LGS implementation of RAVEN (Fig. 7) and show that the RAVEN performance requirements can be met with a system order of 10. The gains achieved as a function of system order are more modest for the NGS-only implementation of RAVEN. In that
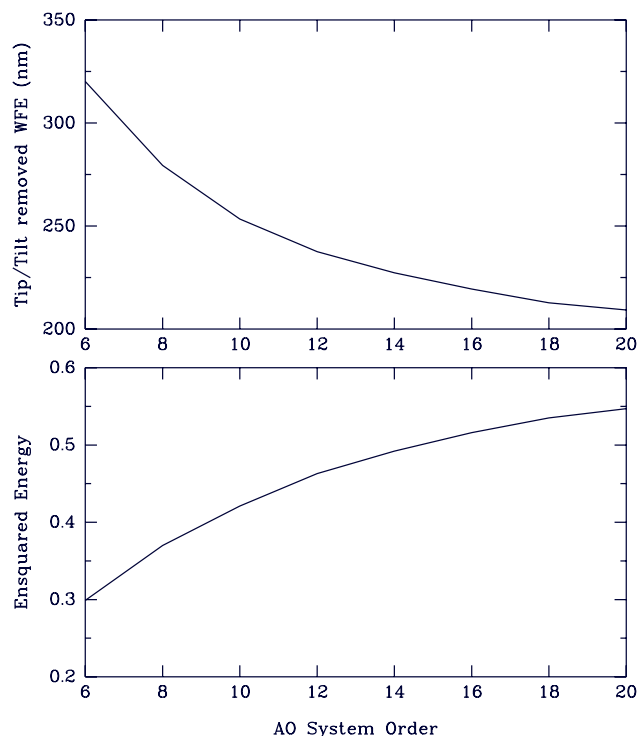

FIG. 7.—Tip/tilt-removed WFE (*top*) and ensquared energy in the *H* band (*bottom*) vs. the system order of RAVEN using three NGSs (on a 45″ diameter ring) and on-axis LGS. Median WFEs and EEs of field points within 45″ of the field center are used. Implementation and WFS noise are included in these simulations. We find that increasing the system order (the number of subapertures across the WFS and number of actuators across the diameter of the DM) will decrease the WFE and increase the EE, but RAVEN will more than meet the performance requirements with a system order of 10 while still allowing for a relatively large collecting area in each subaperture and a higher sky coverage.

case, tomographic error dominates the error budget, so as long as the system order remains greater than ~6, RAVEN performance will not significantly decrease.

4.3.2. WFS FOV

Once the system order had been chosen, the optimal WFS FOV could be determined. We simulated a single OL WFS for different atmospheres with $r_0 = 7, 10$, and 15 cm at a wavelength of 500 nm and an outer scale of $L_0 = 100$ m. Using uncorrelated realizations of the atmosphere, we evaluated the cumulative distribution of source photons within each of the $d_0 = 0.8$ m subapertures. If the IQ is very poor ($r_0 = 7$ cm), one needs a WFS with a FOV approaching $5''$ to not miss light. Under conditions closer to median, a ~$3''$ FOV could suffice.

We also simulated the effect of different outer scales on the required FOV, but found only a very weak dependence. For RAVEN, we chose a FOV of $4.8''$. This should give us some margin if effects other than the atmosphere shift the spots on the WFS.

4.3.3. Plate Scale

Having chosen the system order and set limits on the FOV, the effects of different WFS plate scales on RAVEN performance were examined. To preserve a ~$5''$ WFS FOV, the plate scale needs to be between 0.4 and $0.5''$ pixel^{-1}. At this scale the seeing-limited WFS spots are undersampled, and the concern arises that the sensitivity of the WFS may be compromised. However, simulations indicated that WFE due to the undersampled PSF was only 72 nm for $0.4''$ pixels. This centroiding accuracy was achieved using a MF centroiding algorithm. It is unlikely, however, that an unmodified MF algorithm will be used for centroiding in the RAVEN RTC, because the MF is linear over a limited FOV. We expect to employ either a modified matched-filter algorithm with a moving center defined by the center of gravity or a correlation centroiding algorithm in the RAVEN RTC. We are studying open-loop centroiding in more detail so that errors arising from undersampling the PSF are minimized.

4.4. Performance Using Different Atmospheric Profiles

The performance of the RAVEN AO architecture was benchmarked using the Subaru 50% profile, but the performance of the baseline system was also checked using the Subaru 25% and 75% atmospheric profiles (Table 1). Simulated RAVEN performance for the different profiles, assuming no WFS noise, are presented in Table 6. Even when r_0 is small, RAVEN will still concentrate a significant fraction of the light within the 140 mas IRCS slit.

While the 30% ensquared-energy requirement (under median conditions) will not be met with RAVEN when the IQ is poor, it appears that the performance will gracefully degrade as conditions worsen. If conditions improve, the tomographic error will still dominate the WFE budget. If the central LGS is used, high Strehl ratios (~50%) over a $1.5'$ diameter field can potentially be measured.

4.5. Performance as a Function of Zenith Angle

MOAO performance will depend on the zenith angle of the science target, of course. The distance from each of the atmospheric layers to the telescope is stretched by the air mass, which is equivalent to $\mathrm{AM} \equiv \sec(\gamma)$, and the Fried parameter, r_0, is proportional to $\sec(\gamma)^{-3/5}$. For the LGS, the distance of the generated beacon and the thickness of the sodium layer are also proportional to $\sec(\gamma)$. As a result, the LGS dims in proportion to $\cos(\gamma)$ if we neglect other contributions to LGS
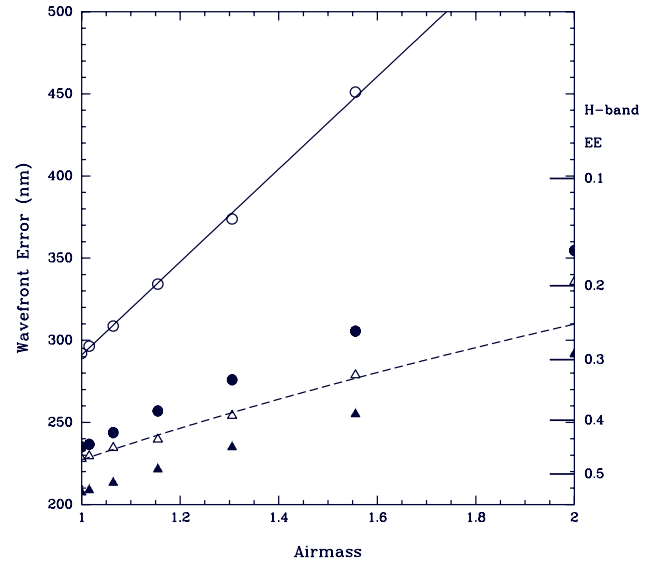
TABLE 6
H-BAND PERFORMANCE FOR DIFFERENT ATMOSPHERIC PROFILES

Subaru IQ profile	LGS + NGS		NGS only	
	EE_{140}	Strehl	EE_{140}	Strehl
25%	0.59	0.48	0.53	0.35
50%	0.51	0.45	0.43	0.29
75%	0.39	0.35	0.30	0.18

FIG. 8.—Wavefront error (*open circles*; scale on left) and *H*-band EE (*filled circles*; scale on right) as a function of air mass for a point near a NGS (*triangles*) and $45''$ from the nearest NGS (*circles*). The performance drops more rapidly for points in the field far from NGSs. At the location of a NGS, the WFE increases as $\mathrm{AM}^{1/2}$.
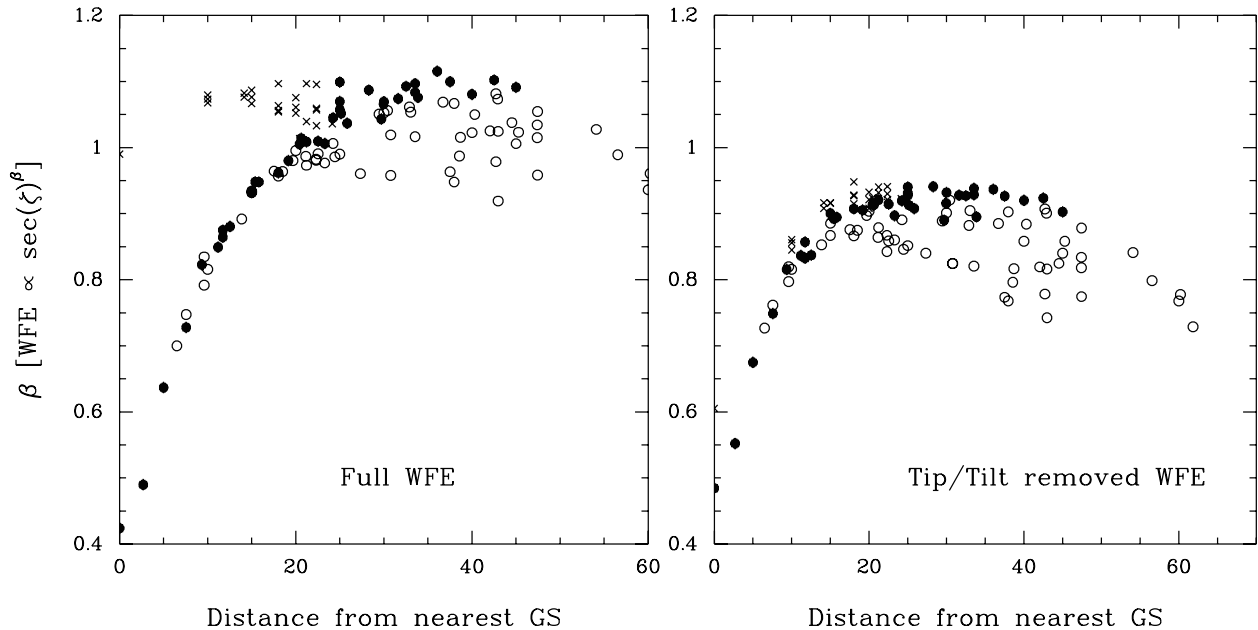
FIG. 9.—Power-law index β, as defined in the relation WFE $\propto \sec \gamma^{\beta}$, vs. distance to the nearest guide star considering the full WFE (*left*) and WFE with the tip/tilt component removed (*right*). Points are labeled by whether the closest guide star is the LGS (x), points are inside the 45″ diameter ring on which the NGSs sit (*filled circles*) or are outside that ring (*open circles*).

brightness, including fasor power and polarization and the Earth's magnetic field (Holzlöhner et al. 2010).

Figure 8 shows the wavefront error and Strehl ratio at the center of the FOR for the baseline RAVEN configuration without the central LGS as a function of air mass. The derived WFEs increase rapidly and are well fit by a power law. Even though the generalized fitting error is a function of the square root of air mass (§ 3.4), we found that the best-fit exponent for a power-law function was greater. One can understand this by considering the overlapping footprints of the guide stars in the metapupils corresponding to different atmospheric layers as the zenith angle changes. As the zenith angle increases, the layers essentially get farther from the telescope, and the metapupils of the guide stars separate, leaving a larger portion of the metapupil for a given layer less well-sampled or even unsensed. If one looks at the power-law index as a function of distance from the nearest guide star, this effect becomes clear (Fig. 9).

For classical AO systems dominated by fitting error, the WFE should be proportional to $AM^{1/2}$. Since a large fraction of the RAVEN WFE budget is dominated by tomographic error, we expect that the power-law index β, defined from the relation WFE $\propto AM^{\beta}$, will vary with distance from the guide stars (Fig. 9). We see that near the NGSs, $\beta \sim 0.5$, but that β rises to ~1 away from the NGSs. The power-law index β is large even very close to the LGS, because atmospheric turbulence is dominated by tip/tilt, which is not sensed by the LGS WFS. If tip/tilt

is excluded, the relation between distance to the guide star and β is virtually indistinguishable between LGSs and NGSs.
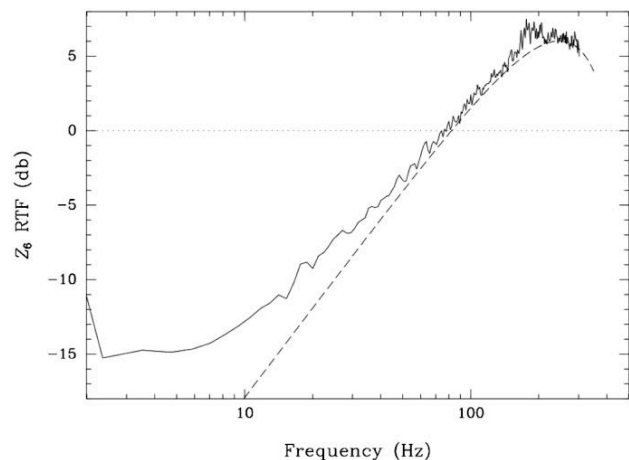

FIG. 10.—VOLT rejection transfer function. The behavior of the RTF at frequencies greater than 40 Hz matches the theoretical OL RTF (*dashed line*), but at low frequencies, the open-loop VOLT system was not making the full rejection. This same behavior is observed with both ViLLaGEs and CANARY.

4.6. Sampling Frequency

ViLLaGEs, VOLT, and CANARY have all demonstrated that open-loop correction is possible. The gain of an open-loop system can be set to unity, because there is no feedback; every wavefront measurement made is applied to the DM. The overshoot is limited to a factor of 2 (because there is no feedback) at one-fourth of the sampling frequency, f_s (assuming a one-frame delay). The correction bandwidth is high; for VOLT running with $f_s = 750$ Hz, the correction bandwidth was approximately 70 Hz (Fig. 10). However, it was also noticed that the RTF flattened out at low temporal frequencies (seemingly independently of spatial frequency). Our best rejection was approximately -15 dB with VOLT (CANARY was able to achieve ~ -25 dB of rejection; E. Gendron 2011, private communication). This is most likely due to some misalignment in the system, which we hope to simulate, but it seems unlikely that this type of error can ever be completely eliminated in RAVEN. Much was learned about alignment and calibration from VOLT, and significant improvement on the OL RTF is anticipated.

To determine the effect that this flattened RTF would have on RAVEN performance, an OL RTF with and without this plateau was simulated. Assumptions made include median image quality of $r_0 = 15.6$ cm at $\lambda = 500$ nm, an infinite outer scale, and a wind speed of 8 m s^{-1}. The residual wavefront error in Zernike modes 7–45 (excluding tip/tilt and second-order radial modes, because errors on these modes will not lead to significant losses in ensquared energy) was measured for different sampling frequencies between 50 Hz $< f_s <$ 500 Hz, different RTF saturation levels of -15 dB and -25 dB, and no saturation (Table 7).

The results are quite independent of sampling frequency, at least above 100 Hz. If RAVEN can be run with $f_s = 100$ Hz, approximately a half-magnitude more can be gained in the limiting magnitude (down to $m_R = 15$ for the NGS-only case), which will in turn have a big impact on the RAVEN sky coverage. It is also noted that saturation levels must be kept at or below -15 dB; at this level, it is already becoming a significant source of WFE. If RAVEN can be kept aligned and calibrated so that this saturation level is approximately -25 dB, the open-loop temporal error will be only a minor contribution to the total WFE budget.

5. SUMMARY AND FUTURE DIRECTIONS

A baseline MOAO system architecture for RAVEN has been established and the expected performance of such a system has been simulated using two independent modeling tools, MAOS and OOMAO. These two independently developed AO simulation tools give excellent agreement for the expected performance of RAVEN. Based on these results, it has been established that RAVEN should be able to meet the design requirement that 30% ensquared energy be delivered within a 140 mas wide IRCS slit if three NGSs are used, and perfor-

TABLE 7
RAVEN OPEN-LOOP TEMPORAL WFE

Saturation level	Sampling frequency				
	50	100	180	250	500
No saturation	91(103)	49(56)	31(36)	25(28)	17(19)
-25 dB	91(105)	52(62)	36(48)	32(45)	28(43)
-15 dB	108(147)	90(134)	88(133)	88(133)	88(133)

NOTES.—Measured in nm rms, excluding first- and second-order Zernike modes. Results in parentheses are residual wavefront errors, excluding only tip and tilt.

mance will improve dramatically if the single Subaru facility on-axis LGS WFS is also included (up to ~40% ensquared energy in median conditions). Employing one LGS beacon also greatly improves the sky coverage, because RAVEN can operate with the LGS in conjunction with just two NGSs that are $m_R < 14.5$ and perhaps even fainter.

A broad spectrum of the system parameter space has been explored. We have looked at RAVEN performance as a function of guide star magnitude. We expect RAVEN to be able to provide the required ensquared energy if the NGSs have magnitude $R < 14.5$ ($R < 15$ if the LGS is also used). Trade studies on the DMs and WFSs have allowed us to settle on an AO system architecture that includes order 10×10 WFSs with a 4.8″ FOV and a pixel scale of $0.4″$ pixel^{-1} and an order 11×11 DM. We explored how the performance changes as the asterism diameter decreases, zenith angle increases, and different atmospheric profiles were used. We found that the degradation of performance with zenith angle is dependent on the distance to the nearest guide star; the farther away the science object sits from a guide star, the more rapidly performance degrades. A study of the performance with sampling frequency using a realistic open-loop rejection transfer function that incorporates the effects of optical misalignments and imperfect calibration concluded that little performance loss is expected if the sampling frequency is greater than or equal to 180 Hz (if the open-loop rejection transfer function plateaus at -15 dB at low temporal frequencies, one has larger wavefront errors, of course, but one can use $f_S = 100$ Hz without additional WFEs).

As the RAVEN project progresses, we are placing a high priority on developing tools to simulate RAVEN alignment and calibration. Exploration of these simulations will improve the understanding of the spatial and temporal frequencies affected by open-loop misalignments. Existing open-loop on-sky experiments reported RTFs that flattened-off at low frequencies. Another issue that needs further study is open-loop centroiding. The MF seems to work quite well under the conditions studied, but concern about a steep dropoff in performance must be addressed in the event that the spots move off of the MF. Thresholded center of gravity should work well in the high-S/N regime, but the sensitivity of the thresholded center of

gravity may be limited, due to the undersampled WFS spots. In addition to these algorithms, we will also explore how well suited correlation centroiding and a modified MF (with a floating center set by the center of gravity) are to open-loop centroiding and RAVEN. Finally, we will continue to explore the feasibility of using advanced control and reconstruction algorithms in the context of RAVEN. We hope that RAVEN will help demonstrate that MOAO projects are indeed feasible and that MOAO instruments are capable of delivering significant multiplex advantages over single-target IFSs.

REFERENCES

Ammons, S. M., Gavel, D. T., Dillon, D. R., Reinig, M., Grigsby, B., & Morzinski, K. M. 2008, Proc. SPIE, 7015, 701546

Ammons, S. M., et al. 2010, PASP, 122, 573

Andersen, D. R., Fischer, M., Conan, R., Fletcher, M., & Véran, J.-P. 2008, Proc. SPIE, 7015, 70150H

Andersen, D. R., Fischer, M., & Véran, J.-P. 2009, OSA Technical Digest, AOThA4

Andersen, D., et al. 2006, Proc. SPIE, 6269, 62694K

Costille, A., et al. 2010, J. Opt. Soc. Am. A, 27, 469

Cuby, J.-G., et al. 2010, Proc. SPIE, 7735, 77352D

Ellerbroek, B. L., Gilles, L., & Vogel, C. R. 2003, Proc. SPIE, 4839, 989

Els, S., et al. 2009, PASP, 121, 527

Flicker, R., Rigaut, F. J., & Ellerbroek, B. L. 2000, Proc. SPIE, 4007, 1032

Gavel, D., Bauman, B., Dekany, R., Britton, M., & Andersen, D. 2006, Proc. SPIE, 6272, 62720R

Gavel, D., et al. 2008, Proc. SPIE, 7015, 70150G

Gendron, E., et al. 2010, Proc. SPIE, 7736, 77360P

Gendron, E., et al. 2011, A&A, 529, L2

Gilles, L., & Ellerbroek, B. 2006, Appl. Opt., 45, 6568

Gilles, L., & Ellerbroek, B. 2008, J. Opt. Soc. Am. A, 25, 2427

Guzmán, D., et al. 2008, Proc. SPIE, 7015, 70153X

Hammer, F., et al. 2002, in Scientific Drivers for ESO Future VLT/VLTI Instrumentation, ed. J. Bergeron, & G. Monnet (Berlin: Springer), 139

Holzlöhner, R., et al. 2010, Proc. SPIE, 7736, 77360V

Jackson, K., Conan, R., & Véran, J.-P. 2010, Proc. SPIE, 7736, 77364K

Johnston, D. C., & Welsh, B. M. 1991, Proc. SPIE, 1542, 76

Kissler-Patig, M. 2010, in 1st Adaptive Optics for Extremely Large Telescopes Conf. (Les Ulis: EDP Sciences), 01001

Martinez, P., et al. 2010, Messenger, 141, 5

Minowa, Y., et al. 2010, Proc. SPIE, 7736, 77363N

Miyashita, A., et al. 2004, Proc. SPIE, 5489, 207

Morris, T., et al. 2010 in 1st Adaptive Optics for Extremely Large Telescopes Conf. (Les Ulis: EDP Sciences), 08003

Morzinski, K., et al. 2010, Proc. SPIE, 7736, 77361O

Nelson, J. 2008, Proc. SPIE, 6986, 698602

Primmerman, C. A., Murphy, D. V., Page, D. A., Zollars, B. G., & Barclay, H. T. 1991, Nature, 353, 141

Puech, M., et al. 2006, NewA Rev., 50, 382

Ragazzoni, R. 1999, in ESO Conf. Proc. 56, Astronomy with Adaptive Optics, ed. D. Bonaccini (Garching: ESO), 651

Ragazzoni, R., Marchetti, E., & Rigaut, F. 1999, A&A, 342, L53

Rigaut, F. J., Ellerbroek, B. L., & Flicker, R. 2000, Proc. SPIE, 4007, 1022

Robin, A. C., Reylé, Derrière, S., & Picaud, S. 2003, A&A, 409, 523 (erratum 416, 157 [2004])

Shectman, S., & Johns, M. 2010, Proc. SPIE, 7733, 77331Y

Tokovinin, A., Le Louarn, M., Viard, E., Hubin, N., & Conan, R. 2001, A&A, 378, 710

Tokunaga, A., et al. 1998, Proc. SPIE, 3354, 512

Vidal, F., et al. 2010, in 1st Adaptive Optics for Extremely Large Telescopes Conf. (Les Ulis: EDP Sciences), E7001V

Wizinowich, P., et al. 2010, Proc. SPIE, 7736, 77360K